Magnetized accretion disks around Kerr black holes with scalar hair - I. Constant angular momentum disks

Sergio Gimeno-Soler,[1] José A. Font,[1,2] Carlos Herdeiro,[3] and Eugen Radu[3]

[1]*Departamento de Astronomía y Astrofísica, Universitat de València, C/ Dr. Moliner 50, 46100, Burjassot (València), Spain*

[2]*Observatori Astronòmic, Universitat de València, C/ Catedrático José Beltrán 2, 46980, Paterna (València), Spain*

[3]*Departamento de Física da Universidade de Aveiro and CIDMA, Campus de Santiago, 3810-183 Aveiro, Portugal*

(Dated: November 16, 2018)

Testing the true nature of black holes – the no-hair hypothesis – will become increasingly more precise in the next few years as new observational data is collected in both the gravitational wave channel and the electromagnetic channel. In this paper we consider numerically generated spacetimes of Kerr black holes with synchronised scalar hair and build stationary models of magnetized thick disks (or tori) around them. Our approach assumes that the disks are not self-gravitating, they obey a polytropic equation of state, the distribution of their specific angular momentum is constant, and they are marginally stable, i.e. the disks completely fill their Roche lobe. Moreover, contrary to existing approaches in the literature, our models are thermodinamically relativist, as the specific enthalpy of the fluid can adopt values significantly larger than unity. We study the dependence of the morphology and properties of the accretion tori on the type of black hole considered, from purely Kerr black holes with varying degrees of spin parameter, namely from a Schwarzschild black hole to a nearly extremal Kerr case, to Kerr black holes with scalar hair with different ADM mass and horizon angular velocity. Comparisons between the disk properties for both types of black holes are presented. The sequences of magnetized, equilibrium disks models discussed in this study can be used as initial data for numerical relativity codes to investigate their dynamical (non-linear) stability and used in tandem with ray-tracing codes to obtain synthetic images of black holes (i.e. shadows) in astrophysically relevant situations where the light source is provided by an emitting accretion disk.

PACS numbers: 95.30.Sf, 04.70.Bw, 04.40.Nr, 04.25.dg

I. INTRODUCTION

In recent years, new families of stationary, asymptotically flat black holes (BHs) avoiding the so-called "no hair" theorems, have been obtained both in general relativity and modified gravity (see e.g. [1] and references therein). Among those, Kerr BHs with synchronised hair [2, 3] are a counterexample to the no hair conjecture resulting from minimally coupling Einstein's gravity to simple (bosonic) matter fields obeying all energy conditions. The physical conditions and stability properties of these classes of *hairy* BHs (HBHs) have been recently investigated to assess their potential viability as alternatives to astrophysical Kerr BHs. On the one hand, Kerr BHs with Proca hair have been shown to form dynamically as the end-product of the superradiant instability [4, 5] (see also [6, 7] for the case of a charged scalar field around a charged BH in spherical symmetry). On the other hand, the stability of these solutions, questioned by [8] in the scalar case, has been recently revisited by [9] who have shown that the domain of HBH solutions for which the superradiant instability might affect their actual existence has no significance for astrophysical BHs, rendering HBHs as *effectively* stable.

In the observational arena, the LIGO/Virgo detection of gravitational waves from binary BHs [10–14] and the exciting prospects of observing the first image – the black hole *shadow* – of a BH by the Event Horizon Telescope (EHT) [15] opens the opportunity to test the true nature of BHs – the no-hair hypothesis – and, in particular, the astrophysical relevance of HBHs. It is not yet known whether the LIGO/Virgo binary BH signals are consistent with alternative scenarios, such as the merger of ultracompact boson stars or non-Kerr BHs, because the latter possibilities remain thus far insufficiently modelled. Likewise, Kerr BHs with scalar hair (KBHsSH) can exhibit very distinct shadows from those of (bald) Kerr BHs, as shown by [16] and [17] for two different setups for the light source, either a celestial sphere far from the compact object or an emitting torus of matter surrounding the BH, respectively. It is therefore an intriguing open possibility if the very long baseline interferometric observations of BH candidates in Sgr A* and M87 envisaged by the EHT may constrain the astrophysical significance of HBHs.

The setup considered by [17] in which the light source producing the BH shadow is an accretion disk, is arguably more realistic than the distant celestial sphere of [16]. Thick accretion disks (or tori) are common systems in astrophysics, either surrounding the supermassive central BHs of quasars and active galactic nuclei or, at stellar scale, surrounding the compact objects in X-ray binaries, microquasars, and gamma-ray bursts (see [18] and references therein). In this paper we present new families of stationary solutions of magnetized thick accretion disks around KBHsSH that differ from those considered by [17]. Our procedure, which combines earlier approaches put forward by [19, 20] was presented in [21] for the Kerr BH case. In Ref. [21] we built equilibrium sequences of accretion disks in the test-fluid approximation endowed with a purely toroidal magnetic field, assuming a form of the angular momentum distribution that departs from the constant case considered by [19] and from which the location and morphology of the equipotential surfaces can be numerically computed. Our goal in the present work is to extend this approach to KBHsSH and to assess the dependence of the morphology and properties of accretion disks on the type of BH considered, either Kerr BHs of varying spins or KBHsSH. In this investigation we focus on disks with a constant distribution of specific angular momentum. In the purely hydrodynamical case, such a model is commonly refereed to as a 'Polish doughnut', after the seminal work by [22] (but see also [23]). In a companion paper we will present the non-constant (power-law) case, whose sequences have already been computed. The dynamical (non-linear) stability of these solutions as well as the analysis of the corresponding shadows will be discussed elsewhere.

The organization of this paper is as follows: Section II presents the mathematical framework we employ to build magnetized disks in the numerically generated spacetimes of KBHsSH. Section III discusses the corresponding numerical methodology to build the disks. Sequences of equilibrium models are presented in Section IV along with the discussion of their morphological features and properties. Finally, our conclusions are summarized in Section V. Geometrized units ($G = c = 1$) are used throughout.

II. FRAMEWORK

A. Spacetime metric and KBHsSH models

The models of KBHsSH we use in this study are built following the procedure described in [24]. The underlying theoretical framework is the Einstein-Klein-Gordon (EKG) field theory, describing a massive complex scalar field Ψ minimally coupled to Einstein gravity. KBHsSH solutions are obtained by using the following ansatz for the metric and the scalar field [2]

$$\mathrm{d}s^2 = e^{2F_1}\left(\frac{\mathrm{d}r^2}{N} + r^2\mathrm{d}\theta^2\right) + e^{2F_2} r^2 \sin^2\theta (\mathrm{d}\phi - W\mathrm{d}t)^2 - e^{2F_0} N \mathrm{d}t^2 \,, \tag{1}$$

$$\Psi = \phi(r,\theta) e^{\mathrm{i}(m\varphi - \omega t)} \,, \tag{2}$$

with $N = 1 - r_{\mathrm{H}}/r$, where r_{H} is the radius of the event horizon of the BH, and W, F_1, F_2, F_0 are functions of r and θ. Moreover, ω is the scalar field frequency and m is the azimuthal harmonic index. We note that the radial coordinate r is related to the Boyer-Lindquist radial coordinate r_{BL} by $r = r_{\mathrm{BL}} - a^2/r_{\mathrm{H,BL}}$, where $a = J/M$ stands for the spin of the BH and $r_{\mathrm{H,BL}}$ is the location of the horizon in Boyer-Lindquist coordinates.

The stationary and axisymmetric metric ansatz is a solution to the EKG field equations $R_{ab} - \frac{1}{2}Rg_{ab} = 8\pi(T_{\mathrm{SF}})_{ab}$ with

$$(T_{\mathrm{SF}})_{ab} = \partial_a\Psi^*\partial_b\Psi + \partial_b\Psi^*\partial_a\Psi - g_{ab}\left(\frac{1}{2}g^{cd}(\partial_c\Psi^*\partial_d\Psi + \partial_d\Psi^*\partial_c\Psi) + \mu^2\Psi^*\Psi\right) \tag{3}$$

where μ is the mass of the scalar field and superscript $(^*)$ denotes complex conjugation. The interested reader is addressed to [24] for details on the equations of motion for the scalar field Ψ and the four metric functions W, F_0, F_1, F_2, along with their solution.

Table I lists the seven KBHsSH models we use in this work. The models have been selected to span all regions of interest in the parameter space. Model I corresponds to a Kerr-like model, with almost all the mass and angular momentum stored in the BH (namely, 94.7% of the total mass and 87.2% of the total angular momentum of the spacetime are stored in the BH), while model VII corresponds to a hairy Kerr BH with almost all the mass (98.15%) and angular momentum (99.76%) stored in the scalar field. It is worth mentioning that some of the models violate the Kerr bound (i.e. the normalized spin parameter is larger than unity) in terms of both ADM or horizon quantities. This is not a source of concern because, as shown in [25], the linear velocity of the horizon, v_{H}, never exceeds the speed of light. For comparison, we also show in the second-to-last column of Table I the spin parameter $a_{\mathrm{H_{eq}}}$ corresponding to a Kerr BH with a horizon linear velocity v_{H}. In the last column, we also include the horizon sphericity of the KBHsSH, defined in [26] as the quotient of the equatorial and polar proper lengths of the event horizon

$$\mathfrak{s} = \frac{L_{\mathrm{e}}}{L_{\mathrm{p}}} = \frac{\int_0^{2\pi} \mathrm{d}\phi e^{F_2(r_{\mathrm{H}},\pi/2)} r_{\mathrm{H}}}{2\int_0^{\pi} \mathrm{d}\theta e^{F_1(r_{\mathrm{H}},\theta)} r_{\mathrm{H}}}. \tag{4}$$

TF: Description of the sphericity. SG: Done In addition to the information provided in Table I, Figure 1 plots the location of our models in the domain of existence of KBHsSH in an ADM mass versus scalar field frequency diagram. TF: This figure has to be redone.

B. Distribution of angular momentum in the disk

Equilibrium models of thick disks around Kerr BHs are built assuming that the spacetime metric and the fluid fields are stationary and axisymmetric (see, e.g. [21, 27, 28] and references therein). For disks around KBHsSH we can follow the same approach as the metric ansatz given by Eq. (1) is stationary and axisymmetric.

We start by introducing the specific angular momentum l and the angular velocity Ω employing the standard

TABLE I. List of models of KBHsSH used in this work. From left to right the columns report the name of the model, the ADM mass, $M_{\rm ADM}$, the ADM angular momentum, $J_{\rm ADM}$, the horizon mass, $M_{\rm H}$, the horizon angular momentum, $J_{\rm H}$, the mass of the scalar field, $M_{\rm SF}$, the angular momentum of the scalar field, $J_{\rm SF}$, the radius of the event horizon, $r_{\rm H}$, the values of the normalized spin parameter for the ADM quantities, $a_{\rm ADM}$, and for the BH horizon quantities, $a_{\rm H}$, the horizon linear velocity, $v_{\rm H}$, the spin parameter corresponding to a Kerr BH with a linear velocity equal to $v_{\rm H}$, $a_{\rm H_{eq}}$, and the sphericity of the horizon, $\mathfrak{s}$.

Model	$M_{\rm ADM}$	$J_{\rm ADM}$	$M_{\rm H}$	$J_{\rm H}$	$M_{\rm SF}$	$J_{\rm SF}$	$r_{\rm H}$	$a_{\rm ADM}$	$a_{\rm H}$	$v_{\rm H}$	$a_{\rm H_{eq}}$	$\mathfrak{s}$
I	0.415	0.172	0.393	0.150	0.022	0.022	0.200	0.9987	0.971	0.7685	0.9663	1.404
II	0.630	0.403	0.340	0.121	0.290	0.282	0.221	1.0140	0.376	0.6802	0.9301	1.352
III	0.797	0.573	0.365	0.172	0.432	0.401	0.111	0.9032	1.295	0.7524	0.9608	1.489
IV	0.933	0.739	0.234	0.114	0.699	0.625	0.100	0.8489	2.082	0.5635	0.8554	1.425
V	0.940	0.757	0.159	0.076	0.781	0.680	0.091	0.8560	3.017	0.4438	0.7415	1.357
VI	0.959	0.795	0.087	0.034	0.872	0.747	0.088	0.8644	3.947	0.2988	0.5487	1.222
VII	0.975	0.850	0.018	0.002	0.957	0.848	0.040	0.8941	6.173	0.0973	0.1928	1.039

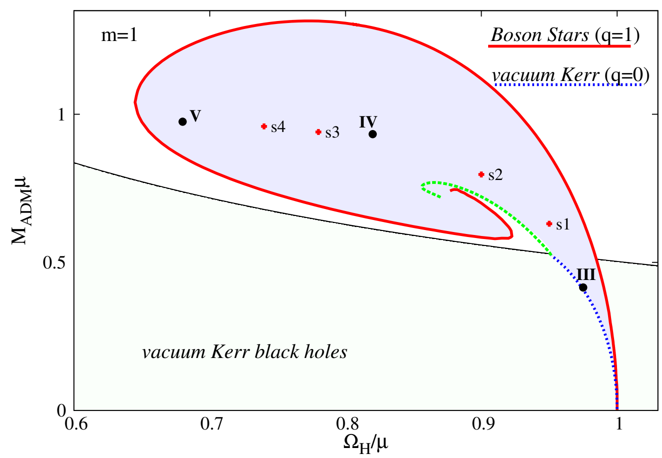

FIG. 1. Domain of existence for KBHsSH in an ADM mass versus scalar field frequency diagram. TF: The figure has to be redone to label the 7 models used in this work.

definitions,

$$l = -\frac{u_\phi}{u_t}, \quad \Omega = \frac{u^\phi}{u^t}, \tag{5}$$

where u^μ is the fluid four-velocity. The relationship between l and Ω is given by the equations

$$l = -\frac{\Omega g_{\phi\phi} + g_{t\phi}}{\Omega g_{t\phi} + g_{tt}}, \quad \Omega = -\frac{l g_{tt} + g_{t\phi}}{l g_{t\phi} + g_{\phi\phi}}, \tag{6}$$

where we are assuming circular motion, i.e. the four-velocity can be written as

$$u^\mu = (u^t, 0, 0, u^\phi)\,. \tag{7}$$

The approach we followed in [21] for the angular momentum distribution of the disks was introduced by [20], and it is characterized by three free parameters, β, γ, and η (see Eq. (7) in [21]). In this work, for simplicity and to reduce the ample space of parameters of the system, we consider a constant angular momentum distribution, $l(r,\theta) = $ const, which corresponds to setting $\beta = \gamma = 0$ in [21]. This choice also allows for the presence of a cusp (and hence matter accretion onto the black hole) and a centre. Following [28], the specific value of the angular momentum corresponding to bound fluid elements ($-u_t < 1$) is computed as the minimum of the following equation

$$l_{\rm b}^{\pm}(r,\theta) = \frac{g_{t\phi} \pm \sqrt{(g_{t\phi}^2 - g_{tt}g_{\phi\phi})(1+g_{tt})}}{-g_{tt}}\,, \tag{8}$$

where the plus sign corresponds to prograde orbits and the minus sign to retrograde orbits. Our convention is that the angular momentum of the BH is positive and the matter of the disk rotates in the positive (negative) direction of ϕ for a prograde (retrograde) disk. Equation (8) is given by [28] for Kerr BHs, but it is valid for any stationary and axisymmetric spacetime. For prograde motion, the function has a minimum outside the event horizon. The location of this minimum corresponds with the marginally bound orbit $r_{\rm mb}$, and the angular momentum corresponds to the Keplerian angular momentum $l_{\rm mb}$ at that point. We show the proof of this statement in Appendix A.

C. Magnetized disks

To account for the magnetic field in the disks we use the procedure described by [19, 29]. First, we write the equations of ideal general relativistic MHD as the following conservation laws, $\nabla_\mu T^{\mu\nu} = 0$, $\nabla_\mu {}^*F^{\mu\nu} = 0$, and $\nabla_\mu(\rho u^\mu) = 0$, where ∇_μ is the covariant derivative and

$$T^{\mu\nu} = (\rho h + b^2)u^\mu u^\nu + (p + p_{\rm m})g^{\mu\nu} - b^\mu b^\nu, \tag{9}$$

is the energy-momentum tensor of a magnetized perfect fluid, h, ρ, p, and $p_{\rm m}$ being the fluid specific enthalpy, density, fluid pressure, and magnetic pressure, respectively, the latter defined as $p_{\rm m} = b^2/2$. The ratio of fluid

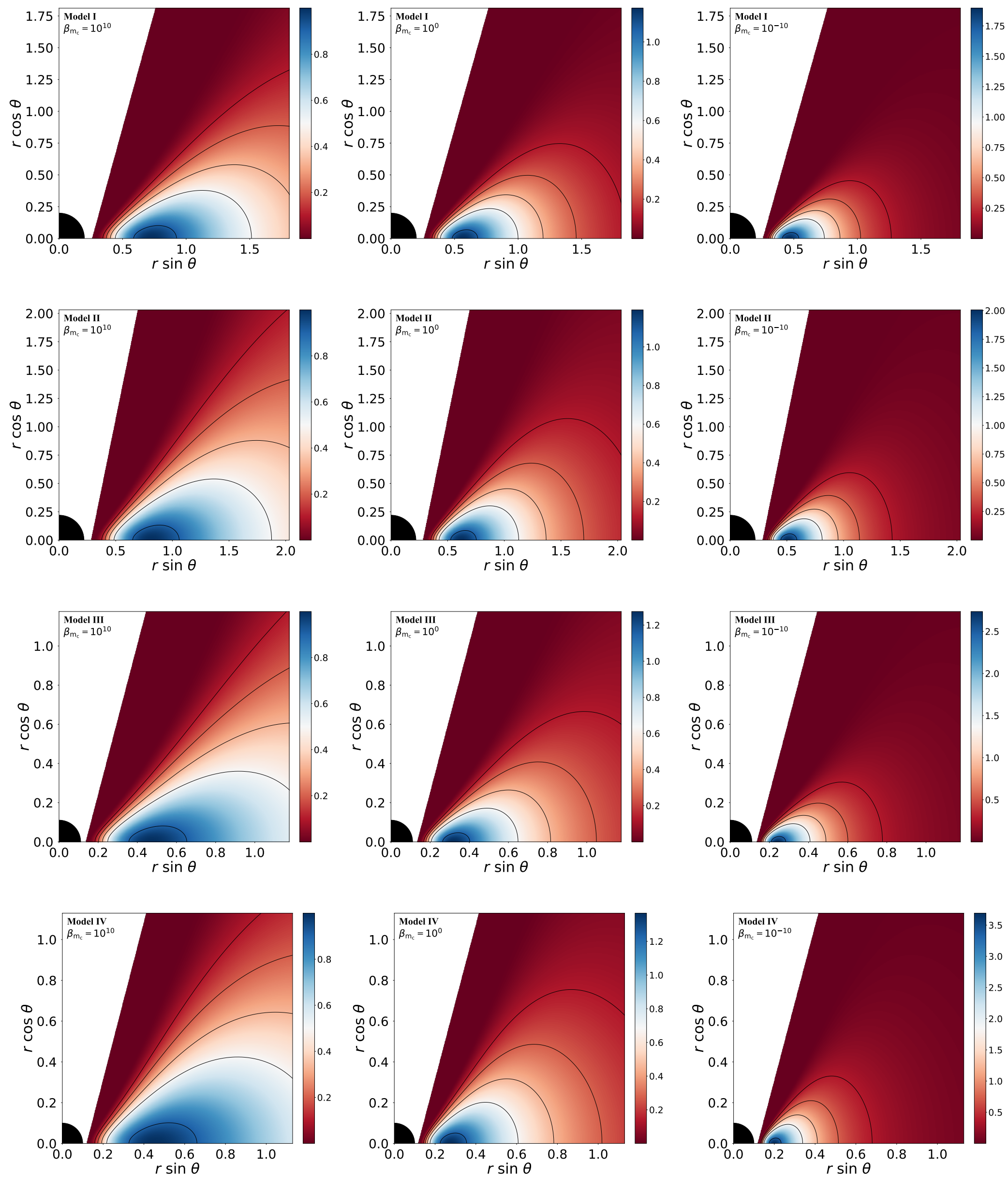

FIG. 2. Distribution of the rest-mass density. From top to bottom the rows correspond to the first four models of KBHsSH (I, II, III and IV). From left to right the columns correspond to different values of the magnetization parameter, namely non-magnetized ($\beta_{\mathrm{m_c}} = 10^{10}$), mildly magnetized ($\beta_{\mathrm{m_c}} = 1$) and strongly magnetized ($\beta_{\mathrm{m_c}} = 10^{-10}$). Note that the range of the colour scale is not the same for all plots.

pressure to magnetic pressure defines the magnetization parameter $\beta_{\mathrm{m}} = p/p_{\mathrm{m}}$. Moreover, ${}^*F^{\mu\nu} = b^\mu u^\nu - b^\nu u^\mu$ is the (dual of the) Faraday tensor relative to an observer with four-velocity u^μ, and b^μ is the magnetic field in that frame, with $b^2 = b^\mu b_\mu$ (see [30] for further details). Assuming the magnetic field is purely azimuthal, i.e. $b^r = b^\theta = 0$, and taking into account that the flow is stationary and axisymmetric, the conservation of the current density and of the Faraday tensor follow. Contracting the divergence of Eq. (9) with the projection tensor $h^\alpha{}_\beta = \delta^\alpha{}_\beta + u^\alpha u_\beta$, we arrive at

$$(\rho h + b^2) u_\nu \partial_i u^\nu + \partial_i \left(p + \frac{b^2}{2} \right) - b_\nu \partial_i b^\nu = 0 \,, \qquad (10)$$

where $i = r, \theta$. This equation can be rewritten in terms of the specific angular momentum l and of the angular velocity Ω,

$$\partial_i (\ln |u_t|) - \frac{\Omega \partial_i l}{1 - l\Omega} + \frac{\partial_i p}{\rho h} + \frac{\partial_i (\mathcal{L} b^2)}{2\mathcal{L}\rho h} = 0 \,, \qquad (11)$$

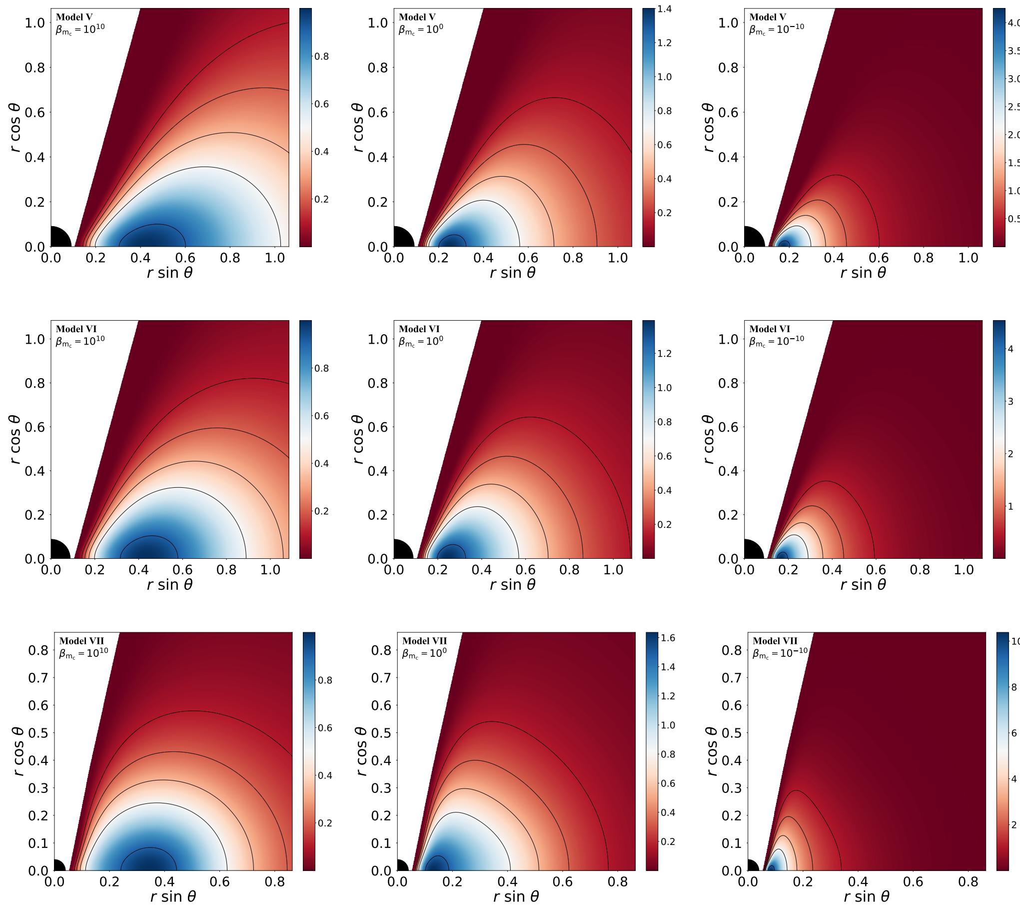

FIG. 3. Same as Fig. 2 but for the last three models of KBHsSH (V, VI, and VII).

where $\mathcal{L} = g_{t\phi}^2 - g_{tt}g_{\phi\phi}$.

To integrate Eq. (11) we need to assume an equation of state (EOS). We assume a polytropic EOS of the form

$$p = K\rho^{\Gamma}, \tag{12}$$

with K and Γ constants. By introducing the definitions $\tilde{p}_{\rm m} = \mathcal{L}p_{\rm m}$, $w = \rho h$ and $\tilde{w} = \mathcal{L}(w)$, we can write equations equivalent to Eq. (12) for both $\tilde{p}_{\rm m}$ and $p_{\rm m}$

$$\tilde{p}_{\rm m} = K_{\rm m}\tilde{w}^q, \tag{13}$$

$$p_{\rm m} = K_{\rm m}\mathcal{L}^{q-1}(\rho h)^q, \tag{14}$$

where $K_{\rm m}$ and q are constants. Then we can integrate Eq. (11) as

$$W - W_{\rm in} + \ln\left(1 + \frac{\Gamma K}{\Gamma - 1}\rho^{\Gamma-1}\right) + \frac{q}{q-1}K_{\rm m}(\mathcal{L}\rho h)^{q-1} = 0, \tag{15}$$

where $W \equiv \ln|u_t|$ stands for the (gravitational plus centrifugal) potential and $W_{\rm in}$ is the potential at the inner edge of the disk.

We can also define the total energy density for the torus, $\rho_{\rm T} = -T^t_t + T^i_i$, and for the scalar field, $\rho_{\rm SF} = -(T_{\rm SF})^t_t + (T_{\rm SF})^i_i$. These are given by

$$\rho_{\rm T} = \frac{\rho h(g_{\phi\phi} - g_{tt}l^2)}{g_{\phi\phi} + 2g_{t\phi}l + g_{tt}l^2} + 2(p + p_{\rm m}), \tag{16}$$

$$\rho_{\rm SF} = 2\left(\frac{2e^{-2F_0}w(w - mW)}{N} - \mu^2\right)\phi^2. \tag{17}$$

Using these expressions, we can compute the total gravitational mass of the torus and the scalar field as the following expression

$$\mathcal{M} = \int \rho\sqrt{-g}\,{\rm d}^3x\,, \tag{18}$$

where g is the determinant of the metric tensor and $\rho \equiv \rho_{\rm T}, \rho_{\rm SF}$.

In this work we take an approach to construct the magnetized disks different to the one proposed by [19] and used by [17] for building disks around KBHsSH. As noted by [21], the approach of [19] implicitly assumes that the specific enthalpy of the fluid is close to unity ($w = \rho h \simeq \rho$). This means that the polytropic EOS Eq. (12) can be written as $p = Kw^{\Gamma}$ (see Eq. (27) of [19]). We do not make this assumption here. To better understand the differences between these two approaches, we consider their behaviour in two limiting cases, namely the non-magnetized case and the extremely magnetized case.

For the former, we can rewrite Eq. (15) in the limiting case of $\beta_{\mathrm{m_c}} \to \infty$ ($K_{\mathrm{m}} \to 0$) as

$$W - W_{\mathrm{in}} + \ln\left(1 + \frac{\Gamma K}{\Gamma - 1}\rho^{\Gamma-1}\right) = 0. \tag{19}$$

Then, we can solve this equation for the specific enthalpy

$$h = e^{W_{\mathrm{in}} - W}. \tag{20}$$

Now, we want to obtain an analogous equation for the $h \simeq 1$ case. We start by considering Eq. (20) of [21] and taking the limit $\beta_{\mathrm{m_c}} \to \infty$ (in this equation, this means $K_{\mathrm{m}} \to 0$), to obtain

$$W - W_{\mathrm{in}} + \frac{\Gamma K}{\Gamma - 1}w^{\Gamma-1}. \tag{21}$$

If we consider the $h \simeq 1$ approximmation, we can use the definition of h and solve the equation to arrive at

$$h = 1 + (W_{\mathrm{in}} - W). \tag{22}$$

If we compare both results, we can see that Eq. (22) is the first-order Taylor series expansion of Eq. (20) for a sufficiently small value of $W_{\mathrm{in}} - W$.

For the extremely magnetised case, we consider again Eq. (15) and Eq. (20) of [21], but this time around we take $\beta_{\mathrm{m_c}} \to 0$ ($K \to 0$). This yields the same result for both equations

$$W - W_{\mathrm{in}} + \frac{q}{q-1}K_{\mathrm{m}}(\mathcal{L}\rho h)^{q-1} = 0. \tag{23}$$

In addition, we could consider the expression for the specific enthalpy in terms of the density $h = 1 + \frac{K\Gamma\rho^{\Gamma-1}}{\Gamma-1}$ to see that we will have $h \to 1$. This shows that, for the extremely magnetized limit, the two approaches coincide.

Taking into account these two limits we can obtain the range of validity of the $h \simeq 1$ approximation: As magnetized disks exist between the two considered cases, for disks with a sufficiently small value of the potential well, $\Delta W \equiv W_{\mathrm{in}} - W_{\mathrm{c}}$, the $h \simeq 1$ approximation is valid. On the contrary, if the value of ΔW is large enough, the approximation does not hold even for disks with a fairly low value of magnetization.

III. METHODOLOGY

We now turn to describe the numerical methodology to build the disks. From the discussion in the preceding section it becomes apparent that the number of parameters defining the disk models is fairly large. In order to reduce the sample, in this work we set the mass of the scalar field to $\mu = 1$, the exponents of the polytropic EOS to $q = \Gamma = 4/3$, the density at the centre of the disk to $\rho_{\mathrm{c}} = 1$, the specific angular momentum to $l = l_{\mathrm{mb}}$ and the inner radius of the disk to $r_{\mathrm{in}} = r_{\mathrm{mb}}$. Thus, we leave the magnetization at the centre, $\beta_{\mathrm{m_c}}$, as the only free parameter for each model of KBHsSH. With this information we can compute all relevant physical quantities.

In particular, our choice of specific angular momentum and inner radius is made to allow disks to have a cusp and a centre. These disks are marginally stable, as they completely fill their Roche lobe, and a small perturbation can trigger accretion onto the BH. In addition, the thermodynamical quantities of the disks reach their maxima for this particular choice of parameters, as they are related to the total potential well $|\Delta W|$. Our choice also implies that the resulting disks will be semi-infinite (they are closed at infinity) but this is not a source of concern, as the external layers of the disk have extremely low density.

Before building the models, it is important to note that we need a sufficiently fine numerical grid to fully capture the behaviour of the physical magnitudes at the innermost regions of the disk. For this reason, we use a non-uniform (r, θ) grid with a typical domain given by $[r_{\mathrm{H}}, 199.2] \times [0, \pi/2]$ and a typical number of points $N_r \times N_\theta = 2500 \times 300$. Those numbers are only representative as the actual numbers depend on the horizon radius r_{H} and on the specific model. The spacetime metric data on this grid is interpolated from the original data obtained by [24]. The original grid in [24] is a uniform (x, θ) grid (where x is a compactified radial coordinate) with a domain $[0, 1] \times [0, \pi/2]$ and a number of points of $N_x \times N_\theta = 251 \times 30$ [31]. To obtain our grid, we use the coordinate transformation provided in [32] and interpolate the initial grid using cubic splines interpolation. An example of our grid is shown in Fig. XXX. TF: We will include this figure if it could be done and were meaningful. TF: Maybe we could also provide the number of the domain and number of points we need for our most extreme case with $a = 0.9999$.

SG: It may be important to note that it seems that we have not angular resolution enough to resolve the morphology of the disk in these extreme cases (see the 2D perimeteral plots). But I think this should go in the results section. TF: I agree with mentioning this in the results section. SG: Added.

To build the disks we first need to find l_{mb} and r_{mb} as the minimum of Eq. (8) and the location of said minimum in terms of the radial coordinate respectively. Once this is done, we can compute the total potential distribution as

$$W(r, \theta) \equiv \ln|u_t| = \frac{1}{2}\ln\left|\frac{g_{t\phi}^2 - g_{tt}g_{\phi\phi}}{g_{\phi\phi} + 2g_{t\phi}l + g_{tt}l^2}\right|. \tag{24}$$

With the total potential distribution, we can compute the location of the cusp r_{cusp} and the centre r_{c} as the extrema (maximum and minimum respectively) of the total potential in the equatorial plane. Also, we set $r_{\mathrm{in}} =$

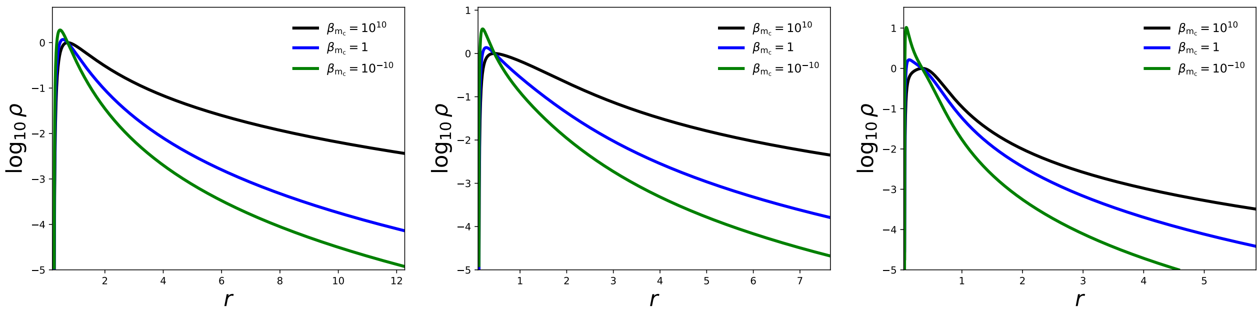

FIG. 4. Size of the disks. Effects of the magnetization on the radial profiles of the logarithm of the density at the equatorial plane for different KBHsSH models. From left to right we show model I, IV, and VII, respectively.

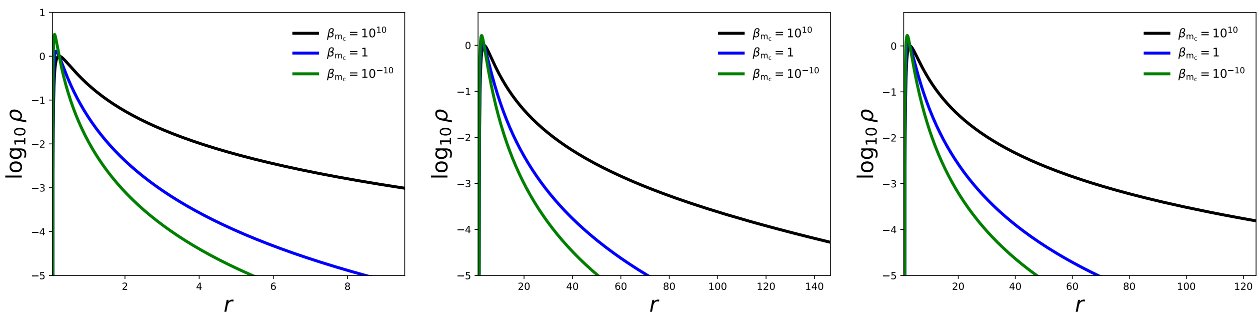

FIG. 5. Size of the disks. Effects of the magnetisation on the radial profiles of the logarithm of the density at the equatorial plane for different KBH models. From left to right we show three different cases with the same ADM quantities as the KBHsSH model I, IV, and VII, respectively.

$r_{\rm cusp}$. For our choice of angular momentum distribution, this also means $W_{\rm in} = 0$. Having the total potential distribution and the characteristic radii of the disk, we can start to compute the thermodynamical quantities in the disk. First of all, we compute the polytropic constant K by evaluating Eq. (15) at the centre

$$W - W_{\rm in} + \ln\left(1 + \frac{\Gamma K}{\Gamma - 1}\rho_{\rm c}^{\Gamma-1}\right) + \frac{q}{q-1}\frac{K\rho_{\rm c}^{\Gamma}}{\beta_{\rm m_c}\left(\rho_{\rm c} + \frac{K\Gamma\rho_{\rm c}^{\Gamma}}{\Gamma-1}\right)} = 0\,, \quad (25)$$

where we have used the definition of magnetic pressure and the definition of the magnetization parameter β. Using their corresponding definitions, we can also compute $h_{\rm c}$, $p_{\rm c}$, $p_{\rm m_c}$ and the constant of the magnetic EOS $K_{\rm m}$. With both K and $K_{\rm m}$ obtained, we can now compute the thermodynamical quantities in all our numerical domain. For points with $W(r,\theta) > 0$ we set $\rho = p = p_{\rm m} = 0$ and for points with $W_{\rm c} < W(r,\theta) < 0$, we write Eq. (15) as

$$W - W_{\rm in} + \ln\left(1 + \frac{\Gamma K}{\Gamma - 1}\rho^{\Gamma-1}\right) + \frac{q}{q-1}K_{\rm m}\left(\mathcal{L}\left(\rho + \frac{K\Gamma\rho^{\Gamma}}{\Gamma-1}\right)\right)^{q-1} = 0\,, \quad (26)$$

to compute the rest-mass density ρ of said point. Then, we can use again Eqs. (12) and (13) and the definition of the specific enthalpy to compute the distribution of p, $p_{\rm m}$ and h.

It is relevant to note that Eqs. (25) and (26) are trascendental equations and that Eq. (26) in particular must be solved at each point of our numerical grid. To solve these equations we use the bisection method. To ensure the accuracy of our computations (particularly the accuracy of the maximum and central quantities we report) we choose our grid to have a difference between two adjacent points of $\Delta r(r \simeq r_{\rm c}) \simeq 0.001$ in the equatorial plane.

IV. RESULTS

A. 2D Morphology

We start presenting the morphological distribution of the models in the $(r\sin\theta, r\cos\theta)$ plane in figures 2 and 3. The radial coordinate employed in these figures is the standard one of the spherical coordinate system. Figures 2 and 3 show the rest-mass density distribution for all our KBHsSH models for 3 different values of the magnetization parameter at the centre of the disks, $\beta_{\rm m_c}$,

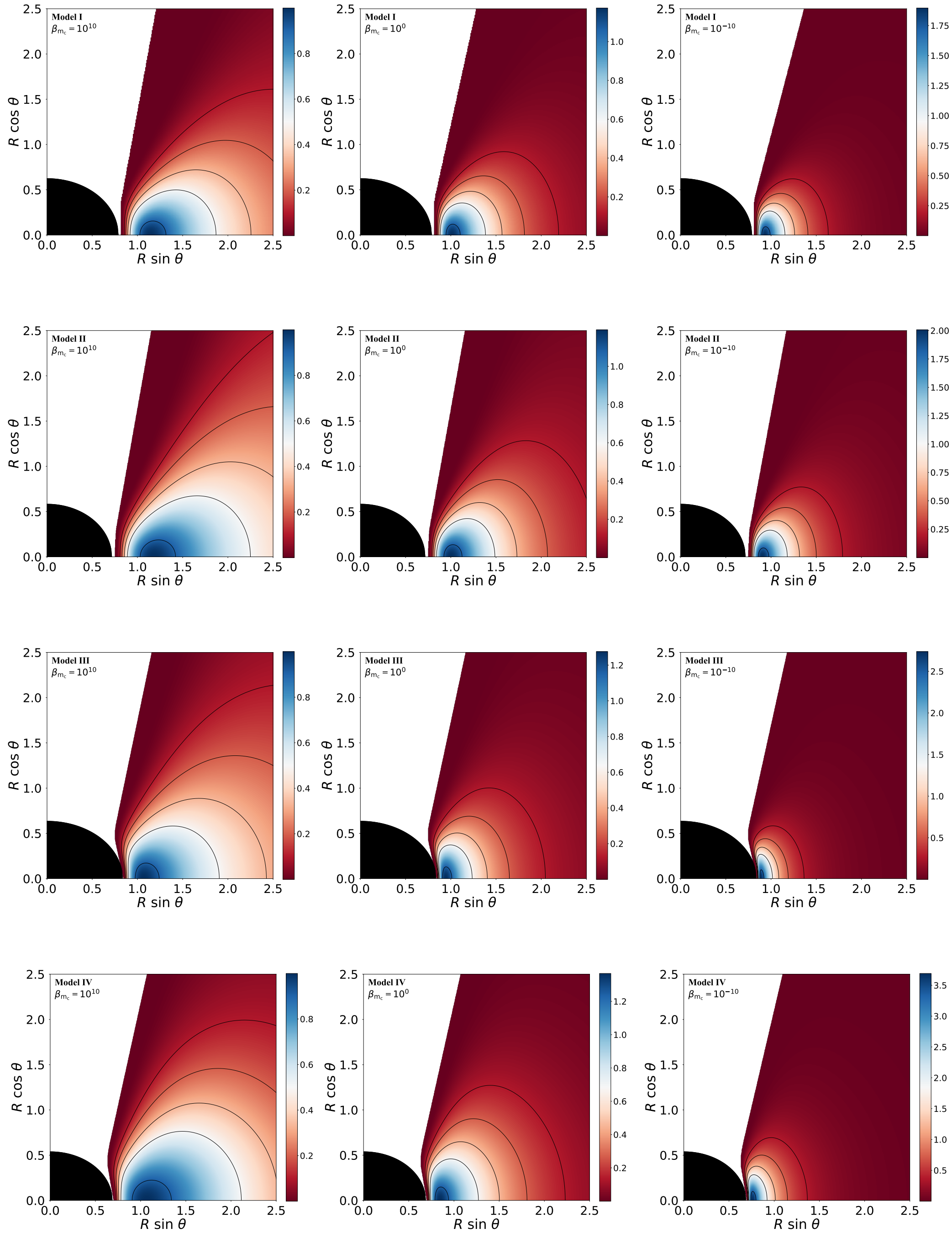

FIG. 6. Same as Fig. 2 but using the perimetral radial coordinate R.

namely 10^{10} (unmagnetized, left column), 1 (mildly magnetized, middle column) and 10^{-10} (strongly magnetized, right column).

The structure of the disks is similar for all values of $\beta_{\mathrm{m_c}}$ with the only quantitative differences being the location of the centre of the disk, which moves closer to the BH as the magnetization increases, and the range of variation of the isodensity contours, whose upper ends become larger with decreasing $\beta_{\mathrm{m_c}}$. This behaviour is in complete agreement with that found for KBHs in [21] irrespective of the BH spin. For the particular case of Model VII, the maximum of the rest-mass density for the strongly magnetized case is significantly larger than for the other models and the spatial extent of the disk is significantly small.

The size of the disks can be best quantified by plotting

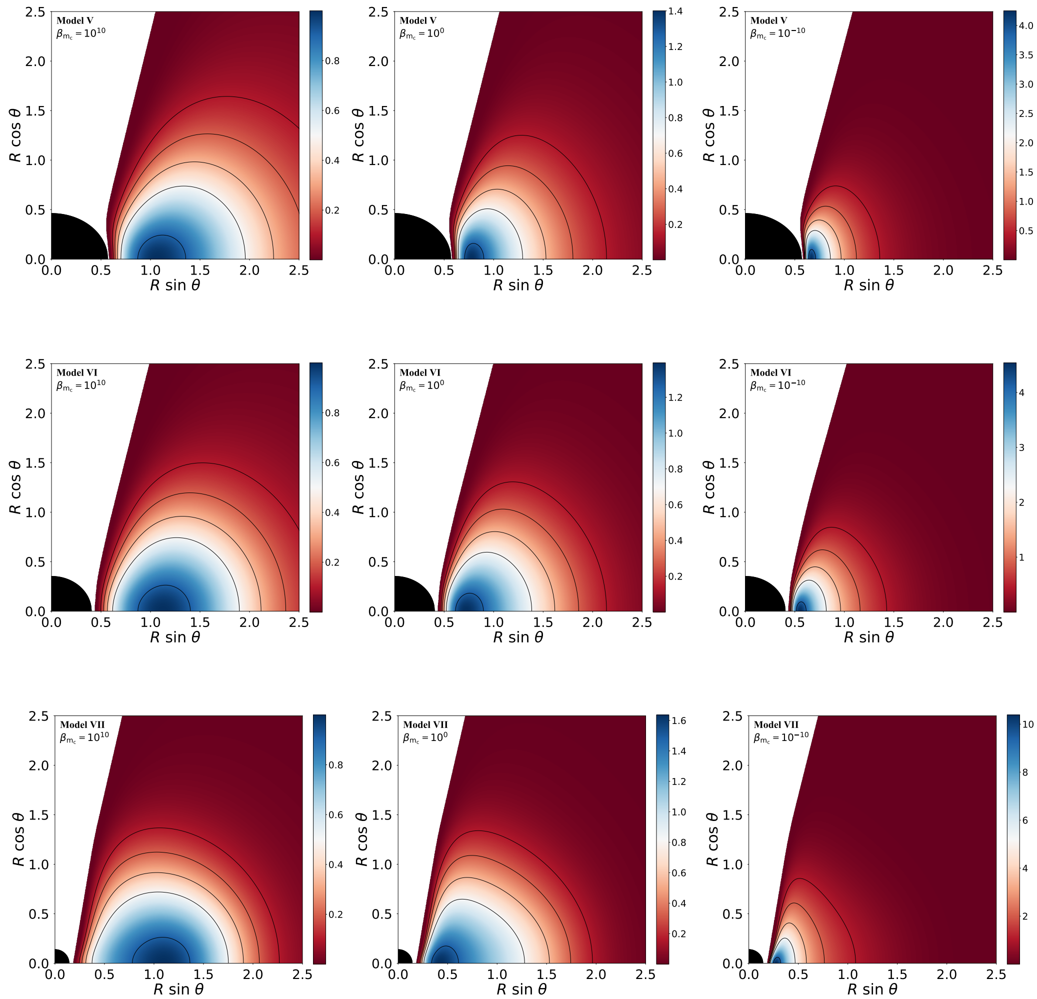

FIG. 7. Same as Fig. 3 but using the perimetral radial coordinate R.

the radial profiles of the rest-mass density on the equatorial plane. This is shown in Fig. 4 for models I, IV and VII and for the same three values of the magnetization parameter shown in Figs. 2 and 3. From this figure we see that model I disks are significantly larger than models IV and VII, i.e. the hairier the models the more compact and smaller they become. We also note the presence of an extended region of high density in the unmagnetized model VII (the mildly-magnetized case also shows this feature but to a lesser extent). This could be related to the existence of an extra gravitational well due to the scalar field distribution that overlaps with the matter distribution of the disk (as can be seen in the right panel of Fig. 8 below).

In figures 6 and 7 we show the same morphological distribution of Figs. 2 and 3 but using, instead, a perimetral radial coordinate R, related to the radial coordinate r according to $R = e^{F_2} r$. This perimetral coordinate represents the proper length along the azimuthal direction, which constitutes a geometrically meaningful direction since it runs along the orbits of the azimuthal Killing vector field. Therefore, the proper size of a full ϕ orbit is given by $2\pi R$, i.e. R is the perimetral radius. The most salient feature of the morphologies shown in Figs. 6 and 7, when comparing to those displayed in Figs. 2 and 3, is the deformation of the disks in their innermost regions. In general, the deformations become larger the higher the horizon sphericity $\mathfrak{s}$ and the closer the disk is to the horizon. Model III is the one showing the largest deformation, as $R_{\rm in} - R_{\rm H}/R_{\rm H}$ attains the smallest value for this model. TF: Check. SG: Done It is also worth noticing that the shape of the BH also changes when using the perimetral coordinate. While in the r coordinate the horizon is spherical (cf. Figs. 2 and 3) in the perimetral coordinate R is not always so. Moreover, the larger the value of $v_{\rm H}$, the more elliptic the horizon becomes, which in our sample corresponds to model III (cf. Table I, $\mathfrak{s} = 1.489$). Also, an interesting property of the perimeteral coordinates is that, for the Kerr metric, $R_{\rm H} = 2M$ irrespective of the value of the angular momentum. But

TABLE II. Values of the relevant physical magnitudes of our models of magnetized, equilibrium tori around KBHsSH. For all cases, $R_{\rm in} = R_{\rm mb}$ and $l = l_{\rm mb}$.

Model	l	$W_{\rm c}$	$R_{\rm in}$	$R_{\rm c}$	$\beta_{\rm m_c}$	$h_{\rm max}$	$\rho_{\rm max}$	$p_{\rm max}$	$p_{\rm m,max}$	$R_{\rm max}$	$R_{\rm m,max}$
I	0.934	−0.188	0.81	1.14	10^{10}	1.21	1.00	5.16×10^{-2}	5.50×10^{-12}	1.14	1.26
					1	1.10	1.17	3.11×10^{-2}	2.68×10^{-2}	1.01	1.06
					10^{-10}	1.00	1.90	1.10×10^{-11}	7.80×10^{-2}	0.93	0.96
II	0.933	−0.205	0.75	1.18	10^{10}	1.23	1.00	5.69×10^{-2}	6.14×10^{-12}	1.18	1.36
					1	1.12	1.19	3.50×10^{-2}	2.97×10^{-2}	1.00	1.07
					10^{-10}	1.00	2.01	1.30×10^{-11}	8.99×10^{-2}	0.91	0.94
III	1.060	−0.362	0.84	1.07	10^{10}	1.44	1.00	1.09×10^{-1}	1.21×10^{-11}	1.07	1.22
					1	1.23	1.28	7.22×10^{-2}	5.76×10^{-2}	0.95	0.99
					10^{-10}	1.00	2.74	3.48×10^{-11}	2.06×10^{-1}	0.89	0.91
IV	1.160	−0.547	0.67	1.06	10^{10}	1.72	1.00	1.82×10^{-1}	2.09×10^{-11}	1.06	1.34
					1	1.38	1.37	1.29×10^{-1}	9.76×10^{-2}	0.85	0.91
					10^{-10}	1.00	3.70	7.83×10^{-11}	4.08×10^{-1}	0.76	0.78
V	1.200	−0.685	0.58	1.07	10^{10}	1.98	1.00	2.46×10^{-1}	2.76×10^{-11}	1.07	1.31
					1	1.51	1.40	1.78×10^{-1}	1.32×10^{-1}	0.78	0.87
					10^{-10}	1.00	4.26	1.18×10^{-10}	5.79×10^{-1}	0.67	0.69
VI	1.200	−0.832	0.43	1.12	10^{10}	2.30	1.00	3.24×10^{-1}	3.52×10^{-11}	1.12	1.32
					1	1.66	1.39	2.28×10^{-1}	1.69×10^{-1}	0.72	0.86
					10^{-10}	1.00	4.54	1.57×10^{-10}	7.40×10^{-1}	0.55	0.59
VII	0.920	−1.236	0.18	1.10	10^{-10}	3.44	1.00	6.10×10^{-1}	6.46×10^{-11}	1.10	1.25
					1	2.25	1.64	5.10×10^{-1}	3.22×10^{-1}	0.43	0.62
					10^{-10}	1.00	10.42	7.03×10^{-10}	2.44	0.28	0.30

for the KBHsSH cases, $2M_{\rm H} < R_{\rm H} < 2M_{\rm ADM}$, and the quotient $R_{\rm H}/2M_{\rm H}$ increases as more mass and angular momentum is stored in the scalar field. SG: It is possible that the angular momentum does not change anything, but we cannot know, as we do not have two different models with the same value of the BH mass.

SG: Discuss. I find that the 2D morphology in perimeteral coordinates might not be very useful, but I found an interesting property of these coordinates: For the Kerr metric, $R_{\rm H} = 2M$ irrespective of the value of the angular momentum (For the KBHsSH cases, $2M_{\rm H} < R_{\rm H} < 2M_{\rm ADM}$. I don't know if there are any kind of dependence on the angular momentum, as we don't two cases with the same value of the mass). I suppose this could help us to compare different models. In fact, the differences in the morphology close to the equatorial plane in the near horizon region are actually related to the value of the angular momentum (we can see a relationship between the morphological differences and the equivalent spin parameter $a_{\rm eq}$). TF: Could you please include some of this information in here? SG: Done

Table II reports the relevant physical quantities for all of our disk models around KBHsSH. It is worth mentioning that KBHsSH can violate the Kerr bound for the potential $\Delta W \equiv W_{\rm in} - W_{\rm c}$. As shown in [22], constant angular momentum disks arround Kerr BHs exhibit a maximum for $|\Delta W|$ when the spin parameter $a \to 1$. This value is $\Delta W_{\rm max} = -\frac{1}{2}\ln 3 \simeq -0.549$. Models V, VI, and VII of our sample violate that bound. As a result, the maximum values of the fluid quantities for disks around KBHsSH are significantly larger than in the Kerr BH case. In both cases, these values increase as $|\Delta W|$ increases, irrespective of the magnetization, as shown in Table II.

In figure 8 we show the total energy density of the torus $\rho_{\rm T}$ (upper half of each image) and the total energy density of the scalar field $\rho_{\rm SF}$ (lower half) for models I, IV and VII and two values of the magnetization parameter at the center (10^{10}, top row, and 10^{-10}, bottom row). This figure shows that, for non-magnetized disks, the maximum of the total energy density of the disk $\rho_{\rm T}$ is closer to the maximum of the total energy density of the scalar field $\rho_{\rm SF}$ for increasing hair. This trend disappears with increasing magnetization, as the disk moves closer to the horizon in such case.

B. Comparison with Kerr BHs

For the sake of comparison we build equilibrium sequences of magnetised disks around four Kerr BHs of varying spins, from $a = 0$ to $a = 0.9999$. Our numerical approach can handle BH spins as large as $|a-1| = 10^{-7}$ without modifying the resolution of our numerical grid. For higher values of the spin parameter, we would need to increase our resolution (specially the θ resolution for the highly magnetised case)SG: DoneTF: Check but such extreme cases do not add further relevant information to

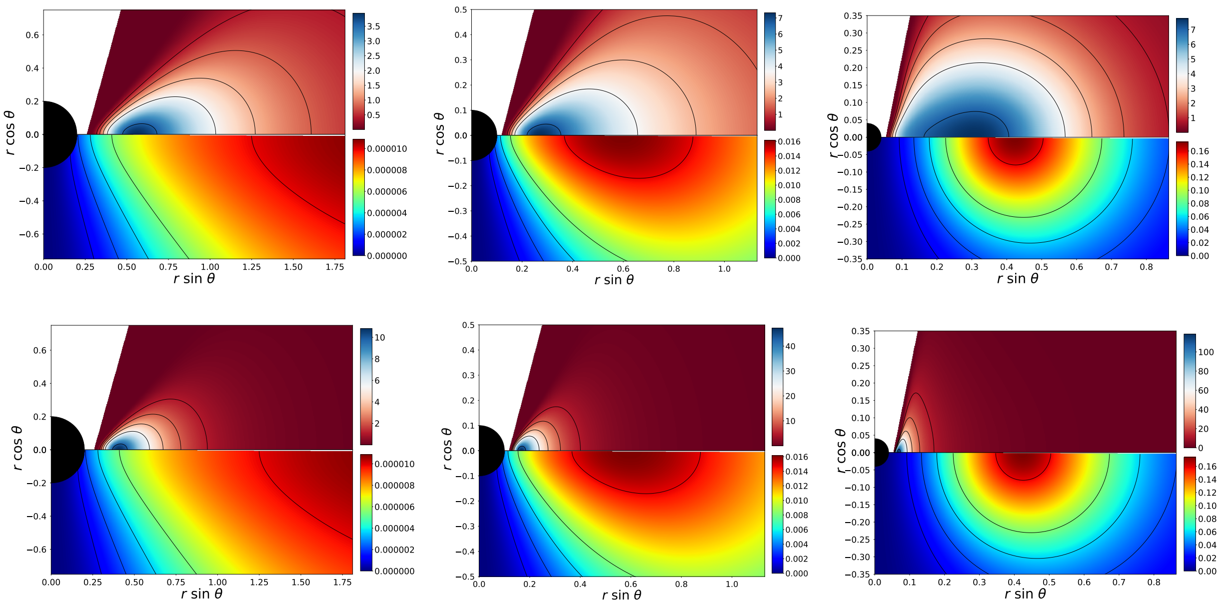

FIG. 8. Energy density distribution for the torus $\rho_{\rm T}$ (upper half of the images) and for the scalar field $\rho_{\rm SF}$ (lower half). From left to right the columns correspond to models I, IV, and VII. The top row corresponds to non-magnetized models ($\beta_{\rm m_c} = 10^{10}$) and the bottom row to strongly magnetized models ($\beta_{\rm m_c} = 10^{-10}$).

TABLE III. Disk parameters and values of their relevant physical magnitudes for the KBH case. For all the cases, we have $R_{\rm in} = R_{\rm mb}$, $l = l_{\rm mb}$ and $M_{\rm BH} = 1$.

a	$\mathfrak{s}$	l	$W_{\rm c}$	$R_{\rm in}$	$R_{\rm c}$	$\beta_{\rm m_c}$	$h_{\rm max}$	$\rho_{\rm max}$	$p_{\rm max}$	$p_{\rm m,max}$	$R_{\rm max}$	$R_{\rm m,max}$
0	1	4.00	-4.32×10^{-2}	4.00	10.47	10^{10}	1.04	1.00	1.10×10^{-2}	1.15×10^{-12}	10.47	11.86
						1	1.02	1.11	6.29×10^{-3}	5.69×10^{-3}	8.81	9.52
						10^{-10}	1.00	1.48	1.83×10^{-12}	1.48×10^{-2}	7.70	8.14
0.5	1.053	3.41	-6.35×10^{-2}	2.99	7.12	10^{10}	1.07	1.00	1.64×10^{-2}	1.72×10^{-12}	7.19	8.14
						1	1.03	1.12	9.43×10^{-3}	8.47×10^{-3}	6.05	6.53
						10^{-10}	1.00	1.53	2.81×10^{-12}	2.23×10^{-2}	5.29	5.59
0.9	1.276	2.63	-0.129	2.18	3.78	10^{10}	1.14	1.00	1.64×10^{-2}	3.65×10^{-12}	3.78	4.23
						1	1.07	1.14	2.03×10^{-2}	1.78×10^{-2}	3.25	3.47
						10^{-10}	1.00	1.70	6.54×10^{-12}	4.92×10^{-2}	2.92	3.04
0.9999	1.629	2.02	-0.429	2.00015	2.034	10^{10}	1.54	1.00	1.34×10^{-1}	1.61×10^{-11}	2.034	2.094
						1	1.29	1.51	1.10×10^{-1}	7.52×10^{-2}	2.0075	2.014
						10^{-10}	1.00	6.17	1.22×10^{-10}	4.91×10^{-1}	2.0021	2.0030

our discussion. Table III reports a summary of the main physical quantities of these disks, whose morphology is displayed in Figs. 9 and 10. As for the disks built around KBHsSH, the maximum values of the enthalpy, density, pressure and magnetic pressure increase with increasing $|\Delta W|$, which, in the Kerr BH case, also means with increasing values of a. It can be seen that both the cusp and the centre move closer to the horizon with increasing a (note that, as we mentioned before in the Kerr case, the radial location of the horizon at the equatorial plane in perimeteral coordinates is $R_{\rm H} = 2M$ irrespective of the value of the spin a). Regarding the physical quantities, we can see that, even for highly rotating KBHs, the maximum values for the h, p and $p_{\rm m}$ are lower than in the KBHsSH case. This is not a surprise, as these quantities are related to the value of $|\Delta W|$. Also, as in the case of KBHsSH, we observe a higher distorsion of the shape of the disc in the near-horizon region with increasing sphericity $\mathfrak{s}$ (and spin, in this particular case). TF: Describe further the table and the figures. TF: Mention that the horizon location is constant in perimetral coordinates irrespective of a. SG: Done

Also, in figures 9 and 10 we show different KBH models with the same mass $M_{\rm BH} = 1$ and different values for the spin parameter(0, 0.5, 0.9, 0.9999). In particular, we can see the well-known behaviour of these models, as the

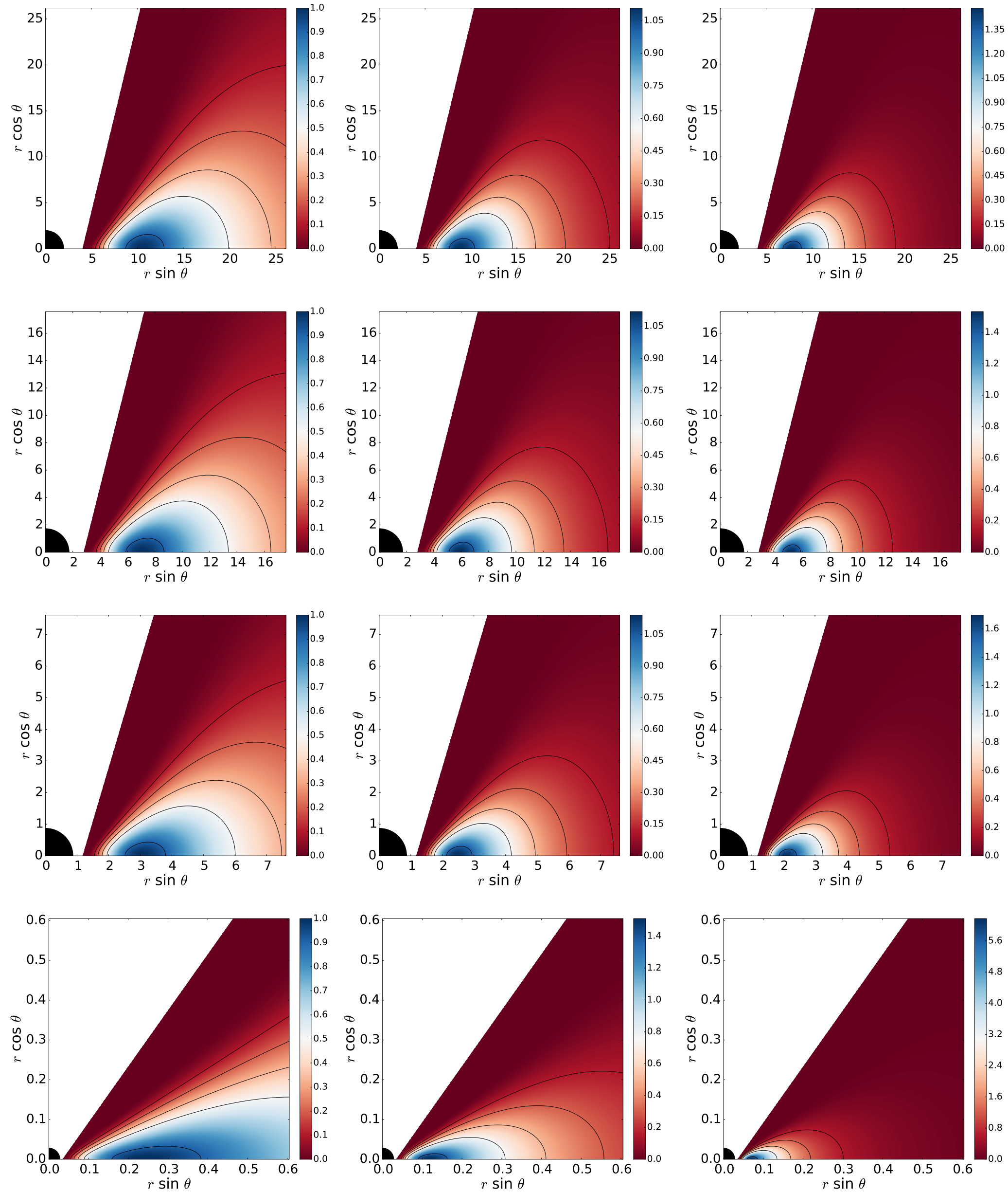

FIG. 9. Rest-mass density distribution. From top to bottom the rows correspond to a sequence of KBHs with increasing spin parameter a (0, 0.5, 0.9 and 0.9999). From left to right the columns correspond to different values of the magnetization parameter, namely non-magnetized ($\beta_{\mathrm{m_c}} = 10^{10}$), mildly magnetized ($\beta_{\mathrm{m_c}} = 1$) and strongly magnetized ($\beta_{\mathrm{m_c}} = 10^{-10}$)

disc reduces its size and tends to attach to the horizon as the spin parameter increases. This cannot be particularly be seen in figure 9, as the radial coordinate expands the near-horizon region and, while it is well suited to do the computations, this is not the case for visualization. However, using perimeteral coordinates (figure 10), we can see the disc attaching to the horizon and the subsequent deformation clearly. SG: complete

In Fig 5, we show three KBH models with the same ADM mass and angular momentum as the cases shown in Fig. 4. The first case corresponds to a near-extremal KBH ($a = 0.9987$) and the other two have a similar value for spin parameter (0.8489 and 0.8941 respectively). Direct comparison between these models and the KBHsSH ones, draws out very interesting features of these models. It can be seen that, for model I, the disc in the Kerr case is considerably smaller than its hairy counterpart. In this case, the scalar field has little effect on the morphology of the disc (as its gravitational field is small), but its effect is noted in a reduction of the value of the sphericity (see Table IV), effectively reducing the effects of the black hole spin in the disc (i.e. increasing its shape). As the mass and angular momentum stored in the scalar field increase, the gravitational field of the scalar field affects

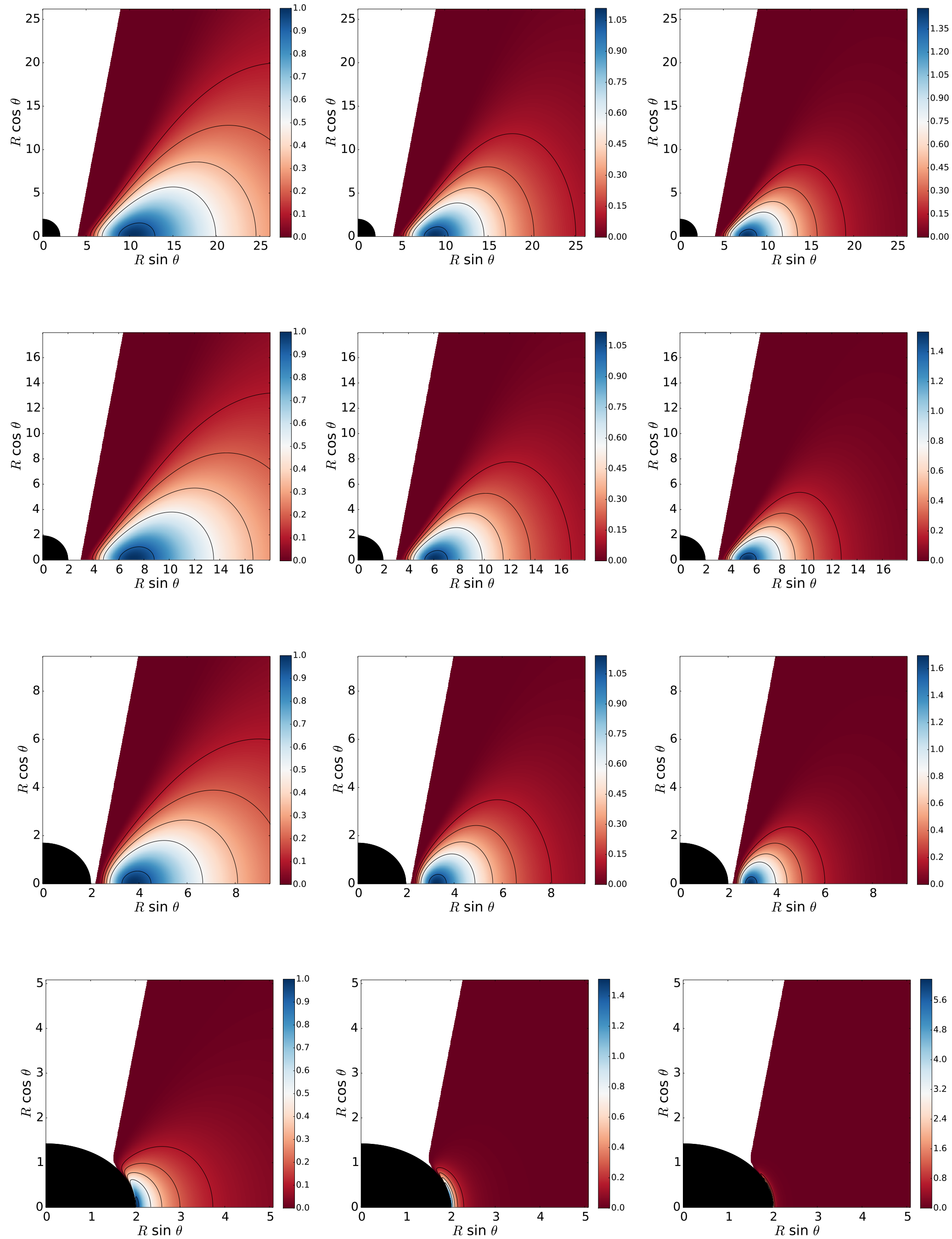

FIG. 10. Rest-mass density distribution using perimeteral coordinates. From top to bottom the rows correspond to a sequence of KBHs with increasing spin parameter a (0, 0.5, 0.9 and 0.9999). From left to right the columns correspond to different values of the magnetization parameter, namely non-magnetized ($\beta_{\mathrm{m_c}} = 10^{10}$), mildly magnetized ($\beta_{\mathrm{m_c}} = 1$) and strongly magnetized ($\beta_{\mathrm{m_c}} = 10^{-10}$)

the radial morphology of the disc, altering its shape and reducing its extent. Note that both model IV and model VII have lesser radial extent than its KBH counterparts, even though model VII has a lower value of the sphericity.

In Table IV, we also present the value of the angular velocity at the disc centre (both for the KBHsSH case and for their KBH counterparts). It can be seen that, with the exception of the first case, the values of the angular velocity of the Kerr cases are lower than SG: I need to think a bit about this.

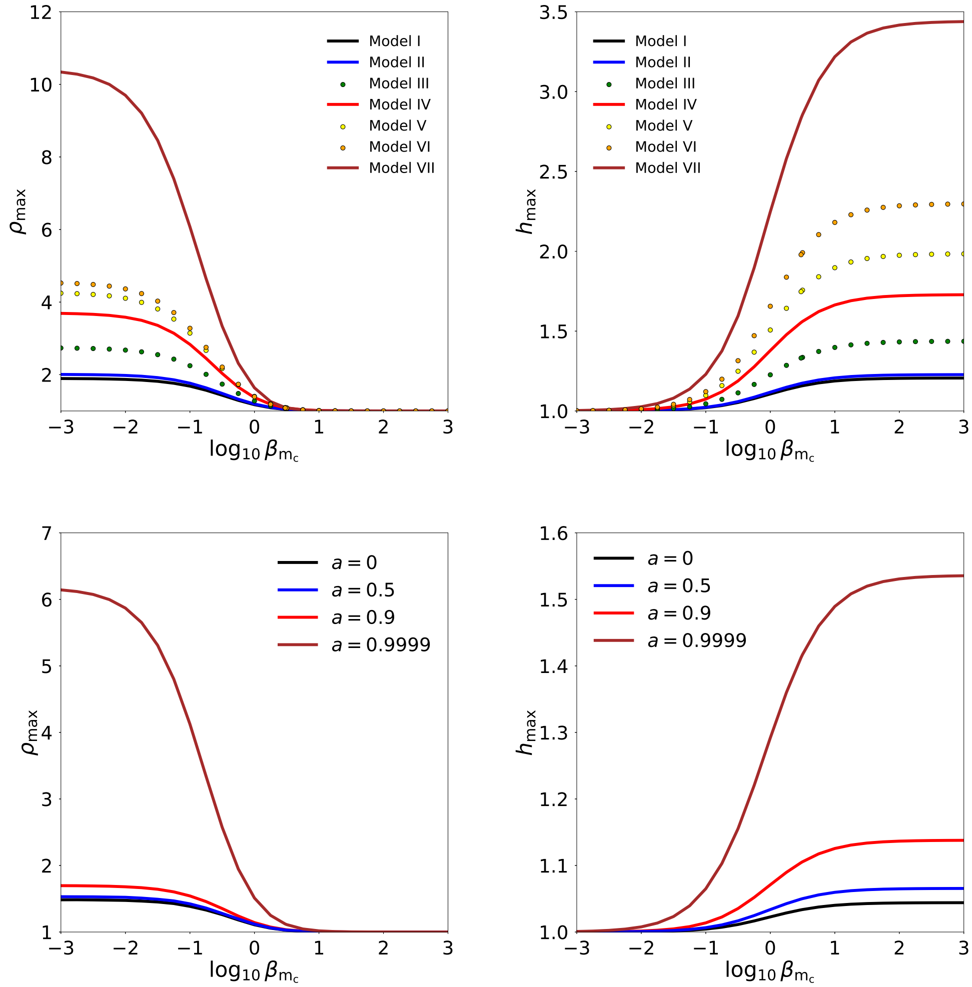

FIG. 11. Effects of the magnetization on the values for the maximum density (left) and enthalpy (right) of the disks. In the first row, we show this for all of our KBHsSH models. In the second row, we show this for a sequence of Kerr BHs with increasing spin parameter. TF: Using yellow is a bad choice as it cannot be seen, especially on print. Please change the colour of the yellow dots to some other colour or symbol.SG: I increased the size of the dots a and added a black edge.

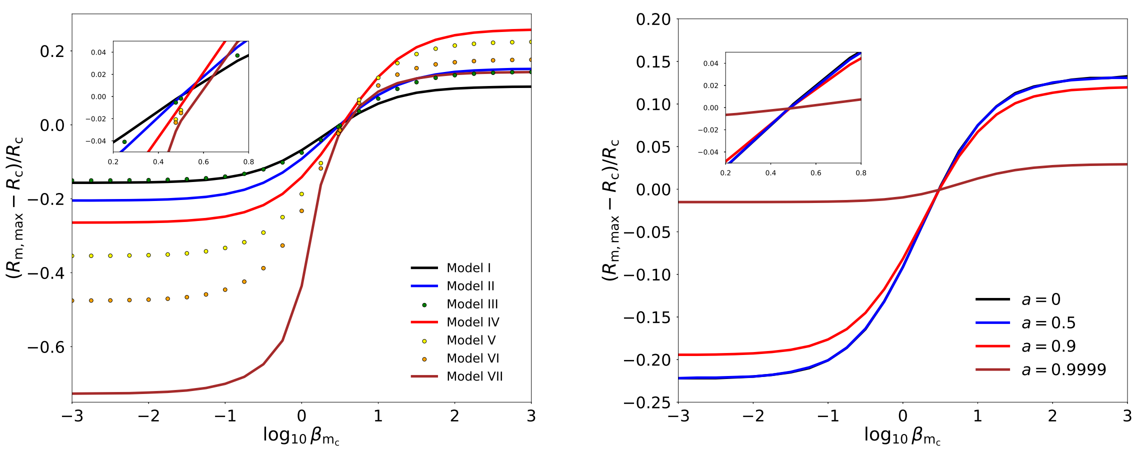

FIG. 12. Effects of the magnetization on the perimeteral location of the magnetic pressure maximum (divided by the the perimeteral radius of the centre), $R_{\mathrm{mag,max}} - R_{\mathrm{c}})/R_{\mathrm{c}})$. Left panel: KBHsSH models. Right panel: A sequence of KBHs with increasing spin parameter. TF: Change the r to R in the vertical labels. SG: Done

TABLE IV. Central density of the disc for the different models, considering a disc with a value of $r_{\rm in}$ such as $\Delta W = 0.9\Delta W_{\rm Total} \equiv W_{\rm cusp} - W_{\rm c}$ and a torus gravitational mass of $M_{\rm T} = 0.1 M_{\rm ADM}$. In the first column, we present the value of the central density for the different KBHsSH models. In the second column, we present the central density for a KBH with the same ADM quantities.SG: complete caption

Model	$\Omega_{\rm c}$	$\beta_{\rm m_c}$	$\rho_{\rm c}$	$\rho_{\rm c}({\rm g\cdot cm^{-3}})$	$\Omega_{\rm ADM_c}$	$\rho_{\rm ADM_c}$	$\rho_{\rm ADM_c}({\rm g\cdot cm^{-3}})$	$\mathfrak{s}_{\rm ADM}$
I	0.493	10^{10}	6.818×10^{-4}	1.739×10^{13}	0.854	3.752×10^{-3}	9.567×10^{13}	1.589
		1	2.185×10^{-3}	5.503×10^{13}		7.942×10^{-3}	2.025×10^{14}	
		10^{-10}	3.227×10^{-3}	8.229×10^{13}		7.641×10^{-3}	1.948×10^{14}	
II	0.424	10^{10}	3.216×10^{-4}	8.201×10^{12}	–	–	–	–
		1	1.651×10^{-3}	4.210×10^{13}	–	–	–	–
		10^{-10}	3.026×10^{-3}	7.716×10^{13}	–	–	–	–
III	0.521	10^{10}	8.120×10^{-4}	2.071×10^{13}	0.163	6.683×10^{-5}	1.704×10^{12}	1.278
		1	3.497×10^{-3}	8.917×10^{13}		2.075×10^{-4}	5.291×10^{12}	
		10^{-10}	5.452×10^{-3}	1.390×10^{14}		3.265×10^{-4}	8.325×10^{12}	
IV	0.427	10^{10}	1.197×10^{-3}	3.052×10^{13}	0.113	3.001×10^{-5}	7.652×10^{11}	1.219
		1	3.421×10^{-3}	8.723×10^{13}		9.512×10^{-5}	2.425×10^{12}	
		10^{-10}	5.135×10^{-3}	1.309×10^{14}		1.533×10^{-4}	3.909×10^{12}	
V	0.394	10^{10}	1.792×10^{-3}	4.569×10^{13}	0.115	3.152×10^{-5}	8.037×10^{11}	1.227
		1	3.883×10^{-3}	9.901×10^{13}		9.942×10^{-5}	2.535×10^{12}	
		10^{-10}	5.435×10^{-3}	1.386×10^{14}		1.596×10^{-4}	4.070×10^{12}	
VI	0.350	10^{10}	2.348×10^{-3}	5.987×10^{13}	0.117	3.232×10^{-5}	8.241×10^{11}	1.234
		1	4.106×10^{-3}	1.047×10^{14}		1.019×10^{-4}	2.598×10^{12}	
		10^{-10}	5.685×10^{-3}	1.450×10^{14}		1.632×10^{-4}	4.161×10^{12}	
VII	0.330	10^{10}	3.737×10^{-3}	9.529×10^{13}	0.129	4.114×10^{-5}	1.049×10^{12}	1.268
		1	5.356×10^{-3}	1.366×10^{14}		1.280×10^{-4}	3.264×10^{12}	
		10^{-10}	7.598×10^{-3}	1.937×10^{14}		2.021×10^{-4}	5.153×10^{12}	

C. Magnetization profiles

The dependence of the maximum specific enthalpy $h_{\rm max}$ and the maximum rest-mass density $\rho_{\rm max}$ with the magnetization parameter is shown in figures 11. The upper panels correspond to the KBHsSH models (I-VII) and the lower ones to our sequence of Kerr BHs with increasing spin parameter. For both cases, an increase in $|\Delta W|$ implies monotonically higher values for $h_{\rm max}$ (low magnetisation) and also higher values for $\rho_{\rm max}$ (high magnetisation). However, there are quantitative differences between the two cases. For the enthalpy, the values of $h_{\rm max}$ reached for disks around KBHsSH are much higher than those of the Kerr BH case. This implies that, while the $w = \rho h \simeq \rho$ approximation (employed in [19, 21]) is valid for magnetized disks ($\beta_{\rm m_c} \sim 1$) around Kerr BHs for values of the spin parameter as high as $a \sim 0.99$, that is not the case for disks around KBHsSH. We note that for the most extreme spin value we can build, $a = 0.9999999$, the maximum enthalpy for the purely hydrodynamical case is $h_{\rm max} = 1.692$. TF: Complete. SG: Done

Figure 12 shows the relative variation of the quotient of the perimetral radius of the magnetic pressure maximum and the perimetral radius of the disk center, $(R_{\rm m,max} - R_{\rm c})/R_{\rm c}$, with the decimal logarithm of the magnetization parameter at the center of the disk, $\log_{10}\beta_{\rm m_c}$. The curves plotted correspond to the same KBHsSH and Kerr BH cases as those in figure 11. For all cases, the radial location of the magnetic pressure maximum decreases with decreasing $\beta_{\rm m_c}$. In [21] we proved that for $h = 1$ disk models in stationary and axisymmetric BH spacetimes, the location of the maximum of the magnetic pressure is identical for all models when $\beta_{\rm m_c} \equiv 1/\Gamma - 1 = 3$. This condition is also fulfilled for the Kerr BH case even when $h \neq 1$, with a slight deviation for cases with very high spin parameter, as can be seen in the inset of the right panel of Fig. 12. However, this condition is not fulfilled for disks built around KBHsSH (see inset in the left panel). At this point, it is relevant to remember that some of the KBHsSH models violate the Kerr bound in terms of the potential. As we mentioned previously, we need a small value of ΔW for the $h \simeq 1$ approximation to be valid in the non-magnetized regime. Now we can see that, in the KBHsSH case, this approximation is not valid even for mildly-magnetized disks.

D. Torus mass

Even though the models we have computed are non self-gravitating, for the sake of astrophysical relevance, we computed the accretion torus mass for the different KBHsSH models and also, for comparison, the torus mass for seven models of Kerr BHs, each one with the same

ADM quantities as their KBHsSH counterparts. For this particular section, we have dropped the $\rho_c = 1$ choice and instead, we have chosen that the mass of the torus must be $M_T = 0.1 M_{ADM}$. Also, to avoid complications due to the infinite size of our models, we have chosen the total potential well as the 90% of its maximum possible value. This is in agreement with the torus masses found as the final state of binary neutron stars mergers (see, for instance [33]). SG: I think we should check and include more references. As we have fixed the value of the mass of the torus, now we have to compute the new value of the central density for each model. In the fourth (KBHSH) and seventh (Kerr) columns of table IV we report the resulting central densities we found. Now, in order to compare our results with the end-product of a binary neutron star merger, we need to convert our result to cgs units. To this end, we first need to choose a mass for the scalar field μ (as the maximum ADM mass of KBHsSH are related to μ). To compute the maximum ADM mass with the followimg equation (see [26] and references therein)

$$M_{ADM}^{max} \simeq \alpha_{BS} 10^{-19} M_\odot \left(\frac{GeV}{\mu}\right) \mathrm{GeV} \qquad (27)$$

for a value of $\alpha_{BS} = 1.315$. Using a value of the mass of $\mu = 2.087 \times 10^{-11}$eV gives us the following values for the ADM mass of our models, from model I to VII (2.043, 3.100, 3.923, 4.592, 4.627, 4.720, 4.799) in units of the mass of the sun $M_\odot$. Note that (as is mentioned in [34]) the value of μ we have chose is compatible with the scalar field mass range allowed by the observational tests in Scalar-Tensor theories. SG: not sure about this last comment, but I think something should be told about μ.

In columns five (KBHSH) to eight (Kerr) of table IV, we report the values of the central density in cgs units we have found for each model. The found values are between $\sim 10^{11}$ and $\sim 10^{14} \mathrm{g} \cdot \mathrm{cm}^{-3}$. This great range is due to the great difference in the disc size for the different models, specially between the Kerr and KBHsSH cases). Comparing these values to the ones in the avalaible literature (see [33] SG: we need more references.) we can see that, considering that our assumptions are quite unrealistic, they are within a reasonable margin of the central densities found in discs as the end-product of numerical simulations of a binary neutron star merger. Changing the rotation law and the EOS to a more realistic one is expected to improve the accuracy of our results.

TF: Sergio please finish this section.

SG: Even the models we have computed are non-self gravitating, for the sake of astrophysical relevance, we computed the mass of some of the disks. For this case only, we have dropped the $\rho_c = 1$ choice and instead, we have chosen that the mass of the torus must be $M_T = 0.1 M_{ADM}$. This is in agreement with the torus masses found as the final state of binary neutron stars mergers

SG: I think here we should go further and do the following: First, choose a suitable maximum ADM mass for the KBHsSH (Eq (I.1) of [3]), this implies a choice of scalar field mass μ. This maximum mass should be such as our models ADM mass would be $\sim 2.5 M_\odot$. Next, we should compute the central density for the models we want to compare (models I, IV, VII for 3 magnetizations and their Kerr ADM equivalents). Finally, we compute the cgs central densities with the formula (From the book of Rezzolla *Relativistic Hydrodynamics*)

$$\rho_{cgs} = 6.17714 \times 10^{17} \left(\frac{G}{c^2}\right) \left(\frac{M_\odot}{M}\right)^2 \rho_{geo} \qquad (28)$$

SG: and compare the central densities (or maximum) with known values.

V. CONCLUSIONS

Astrophysical BHs are commonly surrounded by accretion disks, either at stellar-mass scales or at supermassive scales. In the former case, stellar-mass BHs surrounded by thick disks (or tori) are broadly accepted as natural end results of catastrophic events involving the coalescence and merger of compact objects, namely binary neutron stars and BH-neutron star systems (see e.g. [**?** **?** **?**] and references therein). These systems are traditionally described using the paradigmatic BHs of general relativity, where the spacetime metric is given by the Kerr metric, solely characterized by the BH mass and spin. Upcoming observational campaigns may, however, provide data to discriminate those canonical BH solutions from exotic alternatives as, e.g. those in which the BHs are endowed with scalar or vector (Proca) hair, recently obtained by [2, 3]. It is conceivable that testing the no-hair hypothesis of BHs will become increasingly more precise in the next few years as new observational data is collected in both the gravitational-wave channel and in the electromagnetic channel.

In this paper we have considered numerically generated spacetimes of Kerr BHs with synchronised scalar hair and have built stationary models of magnetized tori around them. Those disks are assumed to be not self-gravitating, to obey a polytropic equation of state, and to be marginally stable, i.e. the disks completely fill their Roche lobe. In addition, and for simplicity purpose, the distribution of the specific angular momentum in the disks has been assumed to be constant. The models have been constructed building on existing approaches presented in [19] and [21]. An important generalization of the present work compared to the methodology presented in previous works has had to do with the fluid model: while the mater EOS is still rather simplistic (a polytropic EOS) the models are allowed to be thermodinamically relativist, as the specific enthalpy of the fluid can adopt values significantly larger than unity. That has led to interesting differences with respect to the findings reported in [21] for the purely Kerr BH case.

We have studied the dependence of the morphology and properties of the accretion tori on the type of BH system considered, from purely Kerr BHs with varying degrees of spin parameter (namely from a Schwarzschild BH to a nearly extremal Kerr case) to KBHsSH with different ADM mass and horizon angular velocity. Comparisons between the disk properties for both types of BHs have been presented. The sequences of magnetized, equilibrium disks models discussed in this study can be used as initial data for numerical relativity codes to investigate their dynamical (non-linear) stability and can be used in tandem with ray-tracing codes to obtain synthetic images of black holes (i.e. shadows) in astrophysically relevant situations where the light source is provided by an emitting accretion disk (first attempted by [17]). In a companion paper we will present the non-constant (power-law) case, whose sequences have already been computed. The dynamical (non-linear) stability of these solutions as well as the analysis of the corresponding shadows will be discussed elsewhere.

ACKNOWLEDGEMENTS

This work has been supported by the Spanish MINECO (grant AYA2015-66899-C2-1-P), by the FCT (Portugal) IF programme, by the CIDMA (FCT) strategic project UID/MAT/04106/2013 and by the European Union's Horizon 2020 research and innovation (RISE) programmes H2020-MSCA-RISE-2015 Grant No. StronGrHEP-690904 and H2020-MSCA-RISE-2017 Grant No. FunFiCO-777740. The authors would like to acknowledge networking support by the COST Action CA16104.

Appendix A: Finding $l_{\rm mb}$ and $r_{\rm mb}$

We start by considering the Lagrangian of a stationary and axisymmetric spacetime

$$L = \frac{1}{2}\left(g_{tt}(\dot{t})^2 + 2g_{t\phi}\dot{t}\dot{\phi} + g_{rr}(\dot{r})^2 + g_{\theta\theta}(\dot{\theta})^2 + g_{\phi\phi}(\dot{\phi})^2\right) \tag{A1}$$

where $\dot{x^\alpha} = \mathrm{d}x^\alpha/\mathrm{d}\lambda$ denotes the partial derivative of the coordinates with respect to an affine parameter λ. We can note that we have two cyclic coordinates (t and ϕ). Then, the canonically conjugate momentum of each coordinate is conserved, namely

$$p_t = \frac{\partial L}{\partial \dot{t}} = -E \tag{A2}$$

$$p_\phi = \frac{\partial L}{\partial \dot{\phi}} = L \tag{A3}$$

where we identify the constants of motion as the energy and angular momentum of a test particle.

If we assume motion in the equatiorial plane (i.e. $\theta = \pi/2$, $\dot{\theta} = 0$) we can write the relativistic four-momentum (of a massive particle) normalisation as

$$p_t p^t + p_r p^r + p_\phi p^\phi = -m^2 \tag{A4}$$

where m is the mass of a test particle. Using the definitions of the energy and angular momentum of the particle and taking into account that $p^\alpha = \dot{x^\alpha}$, we can rewrite the above equation as

$$-E\dot{t} + L\dot{\phi} + g_{rr}\dot{r}^2 = -m^2. \tag{A5}$$

Now, we can find the expressions for the contravariant momenta p^t and p^ϕ from $p_\alpha = g_{\alpha\beta}p^\beta$

$$p^t = \frac{g_{\phi\phi}E + g_{t\phi}}{g_{t\phi}^2 - g_{tt}g_{\phi\phi}} \tag{A6}$$

$$p^\phi = -\frac{g_{tt}L + g_{t\phi}}{g_{t\phi}^2 - g_{tt}g_{\phi\phi}} \tag{A7}$$

now, we can replace these expressions into Eq. (A4) and write the expressin for the radial velocity $\dot{r}$

$$\dot{r} = \left(-m^2 + \frac{g_{\phi\phi}E^2 + 2g_{t\phi}LE + g_{tt}L^2}{g_{t\phi}^2 - g_{tt}g_{\phi\phi}}\right)^{\frac{1}{2}}. \tag{A8}$$

We want to consider circular orbits, so the radial velocity must be $\dot{r} = 0$. Then, we arrive at

$$g_{t\phi}^2 - g_{tt}g_{\phi\phi} = g_{\phi\phi}e^2 + 2g_{t\phi}le + g_{tt}l^2 \tag{A9}$$

where we have introduced the specific energy per unit mass ($e = E/m$) and the specific angular momentum per unit mass ($l = L/m$). Additionally, we are interested in bound orbits. Specifically, we want marginally bound orbits ($e = 1$). Taking this into account, we get the following expression for the specific angular momentum

$$l_{\rm b}^{\pm} = \frac{g_{t\phi} \pm \sqrt{(g_{t\phi}^2 - g_{tt}g_{\phi\phi})(1 + g_{tt})}}{-g_{tt}} \tag{A10}$$

which corresponds to Eq. (8). It is well-known that in black hole spacetimes there is an innermost circular marginally bound orbit for test particles. Naturally, a marginally bound particle at the innermost circular orbit has to have the smallest possible value of the specific angular momentum (i.e. a minimum of Eq. (A10)). The radial location of said minimum is, obviously, the innermost circular marginally bound radius $r_{\rm mb}$.

[1] C. A. R. Herdeiro and E. Radu, International Journal of Modern Physics D **24**, 1542014-219 (2015), arXiv:1504.08209 [gr-qc].

[2] C. A. R. Herdeiro and E. Radu, Physical Review Letters **112**, 221101 (2014), arXiv:1403.2757 [gr-qc].

[3] C. Herdeiro, E. Radu, and H. Rúnarsson, Classical and Quantum Gravity **33**, 154001 (2016), arXiv:1603.02687 [gr-qc].
[4] W. E. East and F. Pretorius, Physical Review Letters **119**, 041101 (2017), arXiv:1704.04791 [gr-qc].
[5] C. A. R. Herdeiro and E. Radu, Physical Review Letters **119**, 261101 (2017).
[6] N. Sanchis-Gual, J. C. Degollado, P. J. Montero, J. A. Font, and C. Herdeiro, Physical Review Letters **116**, 141101 (2016), arXiv:1512.05358 [gr-qc].
[7] P. Bosch, S. R. Green, and L. Lehner, Physical Review Letters **116**, 141102 (2016), arXiv:1601.01384 [gr-qc].
[8] B. Ganchev and J. E. Santos, Physical Review Letters **120**, 171101 (2018), arXiv:1711.08464 [gr-qc].
[9] J. C. Degollado, C. A. R. Herdeiro, and E. Radu, Physics Letters B **781**, 651 (2018), arXiv:1802.07266 [gr-qc].
[10] B. P. Abbott, R. Abbott, T. D. Abbott, M. R. Abernathy, F. Acernese, K. Ackley, C. Adams, T. Adams, P. Addesso, R. X. Adhikari, and et al., Physical Review Letters **116**, 061102 (2016), arXiv:1602.03837 [gr-qc].
[11] B. P. Abbott *et al.* (Virgo, LIGO Scientific), Phys. Rev. Lett. **116**, 241103 (2016), arXiv:1606.04855 [gr-qc].
[12] B. P. Abbott *et al.* (VIRGO, LIGO Scientific), Phys. Rev. Lett. **118**, 221101 (2017), arXiv:1706.01812 [gr-qc].
[13] B. P. Abbott *et al.* (Virgo, LIGO Scientific), Phys. Rev. Lett. **119**, 141101 (2017), arXiv:1709.09660 [gr-qc].
[14] B. P. Abbott *et al.* (Virgo, LIGO Scientific), Astrophys. J. **851**, L35 (2017), arXiv:1711.05578 [astro-ph.HE].
[15] V. Fish, K. Akiyama, K. Bouman, A. Chael, M. Johnson, S. Doeleman, L. Blackburn, J. Wardle, and W. Freeman, Galaxies **4**, 54 (2016), arXiv:1607.03034 [astro-ph.IM].
[16] P. V. P. Cunha, C. A. R. Herdeiro, E. Radu, and H. F. Rúnarsson, Physical Review Letters **115**, 211102 (2015), arXiv:1509.00021 [gr-qc].
[17] F. H. Vincent, E. Gourgoulhon, C. Herdeiro, and E. Radu, Phys. Rev. D **94**, 084045 (2016), arXiv:1606.04246 [gr-qc].
[18] M. A. Abramowicz and P. C. Fragile, Living Reviews in Relativity **16**, 1 (2013), arXiv:1104.5499 [astro-ph.HE].
[19] S. S. Komissarov, MNRAS **368**, 993 (2006), astro-ph/0601678.
[20] L. Qian, M. A. Abramowicz, P. C. Fragile, J. Horák, M. Machida, and O. Straub, A&A **498**, 471 (2009), arXiv:0812.2467.
[21] S. Gimeno-Soler and J. A. Font, Astron. Astrophys. **607**, A68 (2017), arXiv:1707.03867 [gr-qc].
[22] M. Abramowicz, M. Jaroszynski, and M. Sikora, A&A **63**, 221 (1978).
[23] L. G. Fishbone and V. Moncrief, ApJ **207**, 962 (1976).
[24] C. Herdeiro and E. Radu, Classical and Quantum Gravity **32**, 144001 (2015), arXiv:1501.04319 [gr-qc].
[25] C. A. R. Herdeiro and E. Radu, International Journal of Modern Physics D **24**, 1544022 (2015), arXiv:1505.04189 [gr-qc].
[26] J. F. M. Delgado, C. A. R. Herdeiro, and E. Radu, Phys. Rev. D **97**, 124012 (2018).
[27] J. A. Font and F. Daigne, MNRAS **334**, 383 (2002), astro-ph/0203403.
[28] F. Daigne and J. A. Font, MNRAS **349**, 841 (2004), astro-ph/0311618.
[29] P. J. Montero, O. Zanotti, J. A. Font, and L. Rezzolla, MNRAS **378**, 1101 (2007), astro-ph/0702485.
[30] L. Antón, O. Zanotti, J. A. Miralles, J. M. Martí, J. M. Ibáñez, J. A. Font, and J. A. Pons, ApJ **637**, 296 (2006), astro-ph/0506063.
[31] Some samples are presented in [32].
[32] "http://gravitation.web.ua.pt/node/416,".
[33] L. Rezzolla, L. Baiotti, B. Giacomazzo, D. Link, and J. A. Font, Classical and Quantum Gravity **27**, 114105 (2010), arXiv:1001.3074 [gr-qc].
[34] F. M. Ramazanolu and F. Pretorius, Phys. Rev. D **93**, 064005 (2016).